EES Catalysis

PAPER

View Article Online
View Journal | View Issue

Check for updates

Cite this: *EES Catal.*, 2025, 3, 1155

Amino functionalization of the support toward enhanced selective hydrogenation of dimethyl oxalate to methyl glycolate on silver–silicon catalysts†

Guilin Dong, Haiyong Wang, Qian Jiang, Yuhe Liao and Chenguang Wang *

The development of highly efficient catalysts for the selective hydrogenation of dimethyl oxalate (DMO) to methyl glycolate (MG) is an important step in the conversion of syngas into high-value chemicals, which is of great significance for reducing dependence on petroleum and facilitating the transformation of energy structures. Herein three Ag nanoparticles with different size distributions were supported on mesoporous silica nanospheres (MSNS) with uniform center-radial mesopore channels (~7 nm). The effects of the electronic and crystal structures of Ag nanoparticles on the adsorption and activation of DMO and H_2 were studied. The characterization results reveal that amino-functionalization of the support enables the silver–silicon catalyst to possess easily accessible highly dispersed Ag active components, lattice defects which are conducive to the adsorption, activation and diffusion of H_2, as well as electron-rich $Ag^{\delta-}$ species beneficial for the adsorption and activation of DMO, thereby endowing it with high activity, selectivity, and stability. In the reaction of DMO to MG, under the conditions of P = 2.0 MPa, T = 220 °C, H_2/DMO molar ratio = 80, and LHSV = 1.0 h^{-1}, the best catalytic state achieved a DMO conversion of 100%, a MG selectivity of 96.6%, a TOF as high as 207, and the MG yield could still remain above 95% after a 250 h lifetime investigation. Our research highlights a promising route for the development of high-performance Ag catalysts used in the syngas to MG process.

Received 24th April 2025,
Accepted 29th May 2025

DOI: 10.1039/d5ey00123d

rsc.li/eescatalysis

Open Access Article. Published on 30 May 2025. Downloaded on 1/20/2026 4:50:09 AM.
This article is licensed under a Creative Commons Attribution-NonCommercial 3.0 Unported Licence.

Broader context

Due to the wide availability of syngas (CO + H_2) from various sources (such as coal/biomass gasification, natural gas reforming, and CO_2 hydrogenation), the preparation of chemicals using it as a raw material can reduce the reliance on petroleum and is in accordance with the energy diversification strategy. Among them, the hydrogenation of dimethyl oxalate (DMO) from syngas to ethylene glycol (EG) has been industrialized. However, there are still many challenges in obtaining the intermediate product, methyl glycolate (MG), from DMO hydrogenation to EG, such as low catalyst activity, poor selectivity, and high usage of precious metals. Accordingly, we exploited the confinement effect of mesoporous silica nanospheres (MSNS) with mesoporous center-radial channels to fabricate a silver–silicon catalyst, and elaborately discussed the impact of the electronic and crystal structures of silver nanoparticles on the activation of reactants. The characterization results reveal that amino-functionalization of the support enables the silver–silicon catalyst to possess easily accessible highly dispersed Ag active components, lattice defects which are conducive to the adsorption, activation and diffusion of H_2, as well as electron-rich $Ag^{\delta-}$ species beneficial for the adsorption and activation of DMO, thereby endowing it with high activity, selectivity, and stability.

1. Introduction

Methyl glycolate (MG) is an important organic chemical raw material. Due to the two functional groups of hydroxyl and ester, MG has the chemical properties of alcohols and esters, good biocompatibility and degradability, and is widely used in the chemical industry, and in other fields including medicine, fragrances, and polymer materials.[1–8] The existing MG mainly uses petroleum and its derivatives as raw materials, and the preparation methods include carbonylation of formaldehyde, coupling of methyl formate and esterification of chloroacetate, which generally requires a strong acid or base as the catalyst and reaction conditions of high temperature and high pressure, resulting in many side reactions and low yield.[9,10] Therefore, considering the depletion of global oil resources, the uneven

Guangzhou Institute of Energy Conversion, Chinese Academy of Sciences, Guangzhou 510640, P. R. China. E-mail: wangcg@ms.giec.ac.cn

† Electronic supplementary information (ESI) available. See DOI: https://doi.org/10.1039/d5ey00123d

© 2025 The Author(s). Published by the Royal Society of Chemistry

Open Access Article. Published on 30 May 2025. Downloaded on 1/20/2026 4:50:09 AM.
This article is licensed under a Creative Commons Attribution-NonCommercial 3.0 Unported Licence.

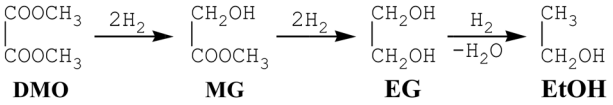

Scheme 1 The reaction pathway for the hydrogenation of DMO.

energy reserves of countries and the requirements of green chemical industrial practices worldwide, the development of a mild route of alternative MG synthesis is of great significance to promote its wide application.

Syngas is a kind of raw gas used for chemical synthesis with hydrogen and carbon monoxide as the main components. It comes from a wide range of sources, including fossil fuels (coal, oil, natural gas), renewable biomass, organic waste, and almost all hydrocarbon feedstocks. Since the synthesis of dimethyl oxalate (DMO) from syngas has been industrialized, selective hydrogenation of DMO to MG under mild reaction conditions using an efficient and easily processed heterogeneous catalyst is a more economical and environmentally friendly non-oil-based process route.[11–13]

The hydrogenation process of DMO is a series reaction. With the deepening of the hydrogenation reaction, the products are MG, ethylene glycol (EG), and ethanol (EtOH) in sequence (Scheme 1).[14,15] At present, Cu-based catalysts have been successfully applied in DMO (derived from syngas) catalytic hydrogenation to EG, and have achieved the industrial production of one million tons of EG per year.[16–19] Due to the high activity of Cu-based catalysts for hydrogenation of the C=O bond, it is easy to deeply hydrogenate DMO to EG, so it is difficult to obtain large quantities of intermediate MG under the existing process conditions, and the yield of MG is generally less than 80%.[20–22] Therefore, the development of highly selective and stable catalysts for DMO selective hydrogenation to MG, and then the efficient use of syngas to produce ethylene glycol devices to achieve product diversification, has become a current research hotspot.

In recent years, more and more research studies have shown that catalysts with Ag as the active component, which has a lower hydrogenation activity than Cu, show a milder hydrogenation performance in the DMO hydrogenation process, and can improve the selectivity and yield of MG.[23,24] In the existing literature, the Ag-based monometallic catalysts used for DMO hydrogenation to MG have higher Ag content (>8 wt%), lower catalytic activity (TOF < 69), and higher cost.[25–28] The research into the Ag-based catalytic system mainly focuses on two directions: first, the use of mesoporous materials instead of traditional silica as the support to increase the dispersion of active components; second, an additive is introduced into the Ag-based catalyst to adjust the electronic state of Ag. However, mesoporous materials, such as SBA-15,[29–31] MCM-41,[27] activated carbon,[32] carbon nanotubes,[25] *etc.*, have a long porous channel (micron level), which is not conducive to mass transfer in the pores.[23] The addition of metal auxiliaries Ni and Co can significantly reduce Ag content. However, Ni can decompose DMO to a certain extent, and the CoAg catalyst is more sensitive to space speed, and the conversion rate drops rapidly to below

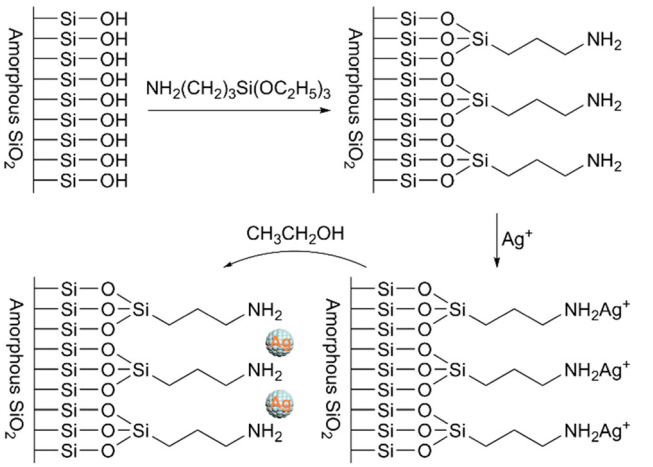

Scheme 2 Main steps in the preparation of our catalysts: surface amination of MSNS is followed by immobilization of Ag nanoparticles onto the aminated MSNS.

70% when the 0.1 h^{-1} space speed increases.[10,29,31] The introduction of nonmetallic elements N and B can effectively regulate the electronic state of Ag, thus generating more active sites. However, due to low Ag dispersion (<0.254), the Ag content in the catalyst is higher than 10 wt%.[32,33]

Previously, we reported that a catalyst loaded with Ag nanoparticles (Ag content < 3 wt%) on mesoporous silica nanospheres (MSNS) showed excellent performance in DMO hydrogenation to MG.[34] Scheme 2 shows the synthesis steps of the catalyst. However, the reason for its high activity was not elaborated. In this study, the effects of electronic and crystal structures of Ag nanoparticles on the adsorption and activation of DMO and H_2 were discussed in detail by comparing silver–silicon catalysts prepared by different methods, and the reason why amino functionalization of the support enhanced the selective hydrogenation of dimethyl oxalate to methyl glycolate on silver–silicon catalysts was explained.

2. Experimental

2.1. Chemicals

Cetyltrimethylammonium chloride (CTAC), triethanolamine (TEA), and 3-aminopropyltrimethoxysilane (APTS) were purchased from J&K Scientific Ltd. Tetraethyl orthosilicate (TEOS), cyclohexane, methylbenzene, ethanol, and silver nitrate ($AgNO_3$) were purchased from Sinopharm Chemical Reagent Co., Ltd. All the reagents were used as received without further purification.

2.2. Preparation of the MSNS support

The MSNS was synthesized *via* a biphasic stratification approach using TEOS as the silica source and CTAC as the template agent, according to a method reported in the literature.[35] Typically, 0.4 g of TEA was dropped into a solution of 15 g of CTAC in 120 mL of deionized water and stirred at 60 °C for 1 h. Then a solution of 7.5 g of TEOS in 25 g of

© 2025 The Author(s). Published by the Royal Society of Chemistry

Open Access Article. Published on 30 May 2025. Downloaded on 1/20/2026 4:50:09 AM. This article is licensed under a Creative Commons Attribution-NonCommercial 3.0 Unported Licence.

cyclohexane was added dropwise to the above solution, and stirred at 60 °C for 12 h. The precipitate after centrifugation was washed with ethanol and dried at 120 °C for 12 h, denoted Sur-MSNS. Then Sur-MSNS was placed in a muffle furnace and calcined at 550 °C for 4 h in static air to remove CTAC, and mesoporous silica nanospheres were obtained, and denoted MSNS. 1.5 g of MSNS were dispersed in 50 g of toluene, then 0.5 g of APTS was added, and refluxed at 110 °C for 12 h. The precipitate after centrifugation was washed with ethanol and dried at 120 °C for 4 h, and the mesoporous silica microspheres with an amino functionalized surface were obtained, denoted NH_2-MSNS.

2.3. Preparation of Ag/NH_2-MSNS and Ag/MSNS catalysts

Using NH_2-MSNS as the support, the catalyst with an Ag loading of 3 wt% was prepared by an *in situ* reduction method. This method uses ethanol as the reducing agent and reduces Ag^+ in the precursor $AgNO_3$ to Ag at 70 °C under normal pressure. Typically, 1.0 g of NH_2-MSNS was ultrasonically dispersed in 90 mL of ethanol. Then, 0.049 g of $AgNO_3$ in 24.5 mL of ethanol was added to the suspension, stirred at 30 °C for 4 h, then heated to 70 °C, and continued to stir for another 4 h until the suspension colour turned brown. The precipitate after centrifugation was cleaned with ethanol and dried at 60 °C for 12 h under a nitrogen atmosphere. Finally, the NH_2-MSNS supported Ag catalyst was obtained, denoted Ag/NH_2-MSNS. For comparison, the Ag catalyst prepared by the same method using MSNS as the support was denoted Ag/MSNS.

2.4. Preparation of Ag/MSNS_im catalysts

The impregnation method is the most commonly used method for preparing supported metal catalysts and is also the method that is widely adopted in the current literature for the preparation of silver–silicon catalysts for the hydrogenation of dimethyl oxalate.[1,25,36] This method requires high-temperature calcination of metal salts to obtain metal oxides, which are then reduced to metals with hydrogen. For comparison, using MSNS as the support, the catalyst with an Ag loading of 3 wt% was prepared by an equivolumetric solution impregnation method. Typically, the volume of water absorbed by 1.0 g of MSNS was determined in advance, and 0.049 g of $AgNO_3$ was dissolved in the measured volume of deionized water, and then a drop of 68 wt% nitric acid solution was added. Then the $AgNO_3$ solution was added to 1.0 g of MSNS in drops and aged for 24 h at room temperature, sheltered from light. After drying at 110 °C for 12 h, calcining at 450 °C for 4 h in static air, and reducing at 350 °C for 4 h under a hydrogen atmosphere, the catalyst with an Ag loading of 3 wt% was obtained, denoted Ag/MSNS_im.

2.5. Catalyst characterizations

Fourier Transform Infrared Spectroscopy (FTIR) was carried out using a Nicolet 6700 spectrometer from Thermo Fisher. The sample (~1 mg) was fully ground with dry KBr (~200 mg) until the particle size was less than 2 μm and pressed into translucent disks at room temperature. The scanning wavenumber range was 4000–400 cm^{-1}, with a resolution of 4 cm^{-1}, a signal-to-noise ratio of 5500 : 1, a wavenumber accuracy of 0.01 cm^{-1}, and 32 scans were performed. The N_2 physical adsorption of the samples was measured at −196 °C using the ASAP 2020 physical adsorption apparatus of micromeritics. All the samples were degassed in vacuum at 200 °C for 3 h to remove the impurities physically adsorbed. The specific surface area (S_{BET}) was calculated by the Brunauer–Emmett–Teller (BET) method, and the mesopore diameter and mesopore volume were calculated by the Barrett–Joyner–Halenda (BJH) method. The actual Ag loading of the samples was determined by using an Agilent 5110 inductively coupled plasma optical emission spectrometer (ICP-OES). Approximately 50 mg of the sample was accurately weighed into a 50 mL polytetrafluoroethylene beaker, and 6 mL of hydrochloric acid, 2 mL of nitric acid, and 4 mL of hydrofluoric acid were added. The beaker was covered and heated at 90 °C for 1 h. The cover was then removed and the solution was evaporated to near dryness. The sample residue was diluted with 5% HNO_3 solution, and the filtrate was made up to 50 mL in a volumetric flask for measurement.

The morphology and structure of the samples were examined using a JEOL JEM-2100F field emission transmission electron microscope (TEM), with an acceleration voltage of 200 kV and equipped with a Gatan GIF Tridium energy filter. Prior to the test, the catalyst samples were ultrasonically homogeneously dispersed in ethanol, and then dropped onto a 200-mesh carbon-supported copper grid and dried thoroughly. The phase characteristics of the samples were characterized using a D8 Advance X-ray polycrystalline diffractometer (XRD) from Bruker AXS. Cu Kα radiation with a wavelength of 0.15418 nm was employed, with an operating voltage of 40 kV and a current of 200 mA. The scanning step size was 0.02°, and the scanning 2θ range was 10° to 80°. The ultraviolet-visible diffuse reflectance spectra (UV-vis DRS) of the samples were acquired by means of the Agilent Cary 5000 ultraviolet-visible-near-infrared spectrophotometer. Barium sulfate ($BaSO_4$), a white standard substance, was adopted as the reference, and the scanning wavelength range was 200 to 800 nm. The surface elemental electronic structure of the samples was analyzed employing the K-alpha X-ray photoelectron spectrometer (XPS) from Thermo Fisher. The Al Kα emission ($h\nu$ = 1486.6 eV) was utilized as the excitation source, and the binding energy of the contaminated carbon C 1s (284.6 eV) was adopted as the external standard for correcting the charging effect of the samples.

The N_2O chemisorption, H_2 temperature-programmed reduction (H_2-TPR), and H_2, DMO, temperature-programmed desorption (H_2-TPD, DMO-TPD respectively) experiments were carried out in a Micrometrics Autochem II 2920 apparatus with a thermal conductivity detector (TCD). For N_2O chemisorption, 100 mg of the solid sample was first reduced at 350 °C under a flow of 50 mL min^{-1} of 10% H_2/Ar for 3 h and then cooled down to 90 °C. Subsequently, the sample was exposed to the pure N_2O (30 mL min^{-1}) for 1 h to ensure that the surface metallic silver atoms were completely oxidized to Ag_2O. The sample was purged with a flow of Ar (30 mL min^{-1}) for 30 min and then cooled down to room temperature under an Ar atmosphere. Next, 10% H_2/Ar (50 mL min^{-1}) was introduced, and the sample was heated up to 800 °C at rate of 10 °C min^{-1}, during which the hydrogen consumption was monitored

Open Access Article. Published on 30 May 2025. Downloaded on 1/20/2026 4:50:09 AM. This article is licensed under a Creative Commons Attribution-NonCommercial 3.0 Unported Licence.

using the TCD.[37] In a typical procedure for the TPD tests, 100 mg of the sample was reduced at 350 °C for 3 h in a 10% H_2/Ar atmosphere, followed by purging with He for 2 h at 300 °C to remove physically adsorbed impurities. After cooling the sample down to 50 °C, a flow of the probe molecule (H_2 for H_2-TPD, DMO for DMO-TPD; for the DMO-TPD experiments the vapor of DMO was carried by Ar) was started until saturated adsorption was reached. The probe molecule was then removed by purging with Ar until the baseline of the MS signal was stabilized. After cooling to room temperature, the TPD profile was collected in Ar from room temperature to 800 °C at a ramping rate of 5 °C min^{-1}. The desorbed probe molecule was monitored by using an online mass spectrometer (MS).

In situ FTIR spectra of DMO adsorbed on the catalysts were recorded using a PerkinElmer Frontier spectrometer and a transmission FTIR cell. Briefly, 30 mg of dried catalyst was compressed into a self-supporting wafer and carefully loaded into the transmission cell. The catalyst was reduced at 350 °C under 5% H_2/N_2 for 3 h and then evacuated by N_2 for 30 min to remove the chemisorbed hydrogen. After cooling down to 80 °C, DMO was evaporated and flowed through the cell with the aid of a vacuum pump for 1 h. That was followed by evacuation to remove any weakly adsorbed DMO. The FTIR spectra were then recorded at the reaction temperature (*i.e.*, 220 °C) with a spectral resolution of 4 cm^{-1} and *via* the accumulation of 64 scans.

2.6. Catalytic evaluation

The catalytic hydrogenation activity assessment of dimethyl oxalate (DMO) was conducted in a stainless steel fixed-bed reactor with an inner diameter of 8 mm. 0.4 g of the catalyst (40–60 mesh) was loaded into the isothermal section of the fixed-bed reactor, and then reduced for 4 hours at 350 °C in a 100 mL min^{-1} H_2 atmosphere to activate the Ag that had been oxidized during storage. At 220 °C and 2 MPa, the DMO in methanol solution (15 wt%) and H_2 with a H_2/DMO molar ratio of 80 was respectively introduced into the evaporator *via* a high-performance liquid chromatography constant-flow pump and a mass flow meter. After being fully mixed in a gas mixer, the mixture was fed into the reactor for the reaction, with a liquid hourly space velocity (LHSV) ranging from 0.2 to 3.0. The outlet gas flow was sampled at intervals of 30 min employing an automatic six-way valve system and subsequently quantitatively analyzed using an online gas chromatograph (Agilent 7890A), featuring a hydrogen flame ionization detector (FID) and a KB-Wax capillary column (30 m × 0.32 mm × 0.25 μm).

The conversion of DMO and the selectivity toward each product were calculated based on the following equations:

$$\text{Conversion}\,(\%) = \frac{\text{mol of DMO (in)} - \text{mol of DMO (out)}}{\text{mol of DMO (in)}} \times 100\%$$

$$\text{Selectivity}\,(\%) = \frac{\text{mol of MG or EG (out)}}{\text{mol of DMO (in)} - \text{mol of DMO (out)}} \times 100\%$$

Turnover frequencies (TOF) were calculated according to the following equation:[38]

$$\text{TOF} = \frac{W \times V \times C_{\text{DMO}}}{D \times N_{\text{Ag}}}$$

where W is the DMO concentration in the DMO/methanol solution (mol L^{-1}), V is the flow rate of the DMO/methanol solution (L h^{-1}), C_{DMO} is the DMO conversion, N_{Ag} is the total amount of Ag (mol) in the used catalyst and D is the Ag dispersion obtained from N_2O chemisorption and H_2-TPR measurements. To obtain the TOF values, the reaction was performed at 2.4, 4.5 and 12.0 h^{-1} of LHSV for Ag/MSNS_im, Ag/MSNS and Ag/NH_2-MSNS, respectively, while the other reaction conditions were kept at the same levels (T = 220 °C, P = 2.0 MPa and H_2/DMO = 80) to ensure that the conversion of DMO is below 20%.

3. Results and discussion

3.1. Structure and physical properties of supports

Fourier transform infrared spectroscopy (FTIR) results of Sur-MSNS containing template agent, MSNS removing template agent, and NH_2-MSNS with surface amination are shown in Fig. 1a.

The absorption peaks of the three curves at 3424 cm^{-1}, 1626 cm^{-1}, 1090 cm^{-1}, 800 cm^{-1} and 468 cm^{-1} are respectively attributed to the antisymmetric stretching vibration peak of OH in Si–OH, the H–O–H bending vibration peak of water, the antisymmetric stretching vibration peak of Si–O–Si, the symmetric stretching vibration peak and the bending vibration peak of the Si–O bond. In addition, at 800 cm^{-1} and 690 cm^{-1}, there are no double peaks and sharp peaks of Si–O bond symmetric stretching vibration in crystalline SiO_2. The results show that the catalyst supports are mainly composed of amorphous SiO_2 covered by Si–OH groups. The absorption peaks of Sur-MSNS at 2924 cm^{-1} and 2850 cm^{-1} are attributed to the antisymmetric and symmetric stretching vibration of CH_2, respectively, and the absorption peak at 1460 cm^{-1} is attributed to the symmetric variable angle vibration of CH_2. The weak absorption peak at 1408 cm^{-1} is attributed to the symmetric variable angle vibration of CH_2 in $-CH_2-N^+$. It can be seen that Sur-MSNS without roasting contains the template agent CTAC. The absorption peaks of roasted MSNS almost disappeared at 2924 cm^{-1}, 2850 cm^{-1}, 1460 cm^{-1} and 1408 cm^{-1}, indicating that the template agent CTAC could be effectively removed by roasting at 550 °C for 4 hours. After surface amination modification, NH_2-MSNS re-generated absorption peaks at 2924 cm^{-1}, 2850 cm^{-1} and 1460 cm^{-1}, indicating that the surface of MSNS contained CH_2 groups, which came from the organic carbon chain of APTS. At the same time, the weak absorption peaks of NH_2-MSNS at 1562 cm^{-1} and 700 cm^{-1} are attributed to the plane shear vibration and the out-of-plane rocking vibration of NH, respectively, indicating that the surface of NH_2-MSNS contains $-NH_2$ groups. In addition, the full range XPS spectra of NH_2-MSNS shows that its surfaces contain N (Fig. 1b). The above results show that the acetal reaction takes place between the hydroxyl group on the surface of MSNS and the ethoxy group of

© 2025 The Author(s). Published by the Royal Society of Chemistry

Open Access Article. Published on 30 May 2025. Downloaded on 1/20/2026 4:50:09 AM.
This article is licensed under a Creative Commons Attribution-NonCommercial 3.0 Unported Licence.

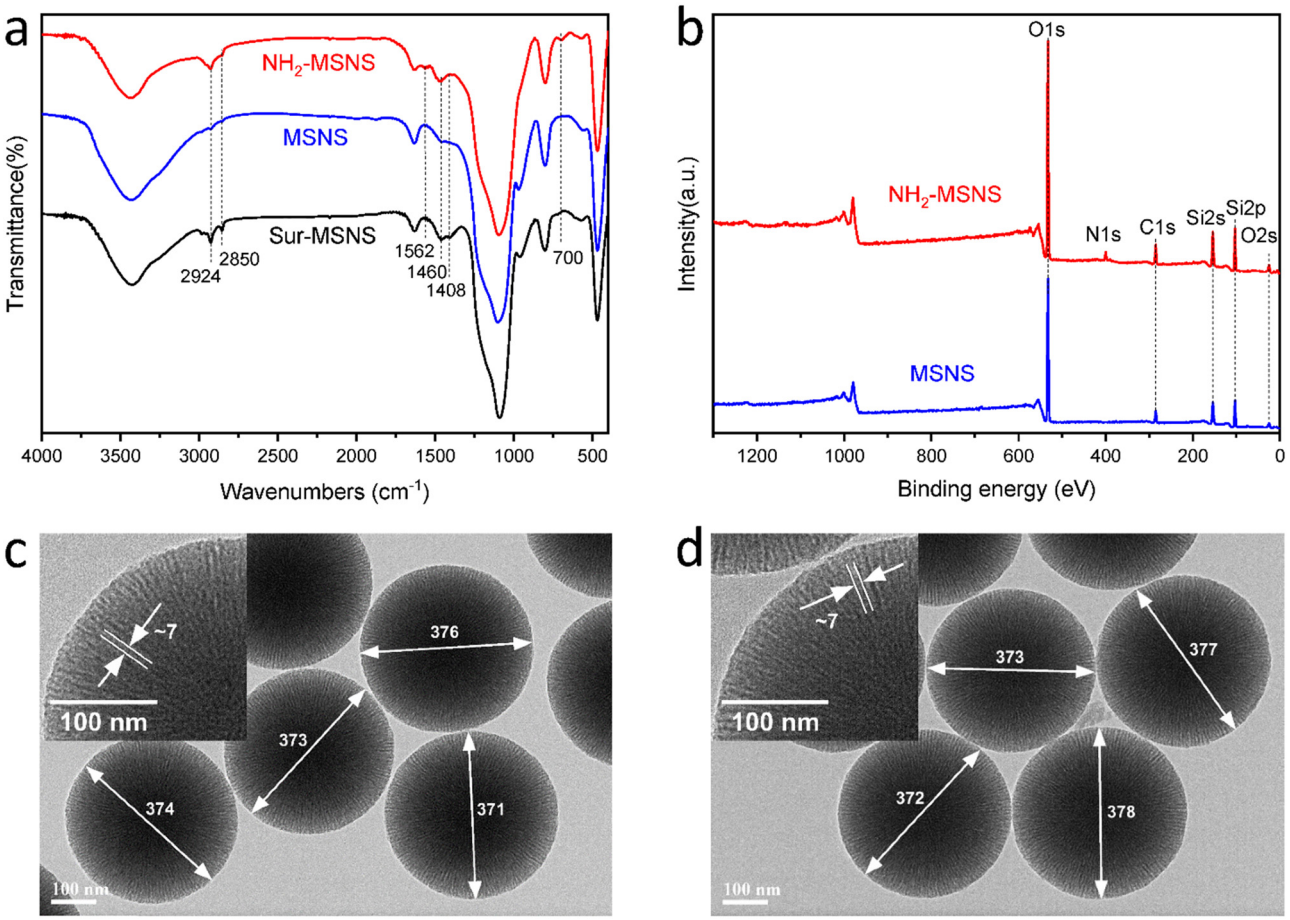

Fig. 1 (a) FTIR spectra of Sur-MSNS, MSNS, and NH_2-MSNS. (b) Full range XPS spectra of MSNS and NH_2-MSNS. TEM and inset HR-TEM images of (c) MSNS and (d) NH_2-MSNS.

APTS, and the surface of MSNS is covered by aminopropyl groups, and the surface amination modification of NH_2-MSNS is obtained.

Transmission electron microscopy (TEM) images of MSNS without template agent and NH_2-MSNS with surface amination are shown in Fig. 1c and d, respectively. It can be seen that both the MSNS and NH_2-MSNS have good dispersion, the particle size is uniform, the diameter is about 370 nm, the pore channel is a center divergent slit, and the pore size is about 7 nm. Compared with MSNS, NH_2-MSNS has no obvious difference in microstructure. It can be seen that the surface amination of MSNS does not destroy the original microstructure.

The N_2 adsorption–desorption isotherms of the supports and catalysts and their BJH pore size distribution curves are shown in Fig. 2. N_2 adsorption isotherms of NH_2-MSNS and MSNS are a combination of type II and type IV isotherms, and hysteresis rings belong to type H3 (Fig. 2a). The pore structure of the sample is a wedge slit hole formed by agglomeration of sheet particles, which is consistent with the TEM observation results. The shape of isotherms and hysteresis rings is basically the same, which further indicates that the surface amination modification does not damage the particle structure. Among them, the BJH pore size distribution of MSNS is slightly wider (4–10 nm), which may be caused by the narrow inside and wide outside channel structure of the wedge-shaped slit holes (Fig. 2b). Compared with MSNS, the position, area and pore size distribution of the NH_2-MSNS hysteresis ring are all shifted in the negative direction, indicating that the pore volume and pore size of NH_2-MSNS are reduced to some extent by the introduction of aminopropyl. As shown in Table 1, the specific surface area, pore volume and pore size of MSNS are 665 $m^2\ g^{-1}$, 0.80 $m^3\ g^{-1}$ and 6.61 nm, respectively, while for NH_2-MSNS, they are reduced to 323 $m^2\ g^{-1}$, 0.41 $m^3\ g^{-1}$ and 6.17 nm respectively. It is worth noting that the pore size distribution of NH_2-MSNS is narrower (5–7 nm), and the possible reason is that the surface modification makes the wide-outside and narrow-inside wedge-shaped slit channels in MSNS tend to be uniform (cylindrical holes) (Fig. 2b).

The above results showed that the surface of MSNS was successfully modified with silane coupling agent APTS, and aminopropyl groups were introduced onto the surface, and NH_2-MSNS with amination was obtained. At the same time, MSNS is a good support for catalyst preparation due to its high specific surface area, short pore size and uniform nano pore size.

3.2. Structure and physical properties of the catalysts

The Ag content of catalyst after the ICP-OES test is shown in Table 1. The actual Ag content of Ag/MSNS_im is essentially

Open Access Article. Published on 30 May 2025. Downloaded on 1/20/2026 4:50:09 AM.
This article is licensed under a Creative Commons Attribution-NonCommercial 3.0 Unported Licence.

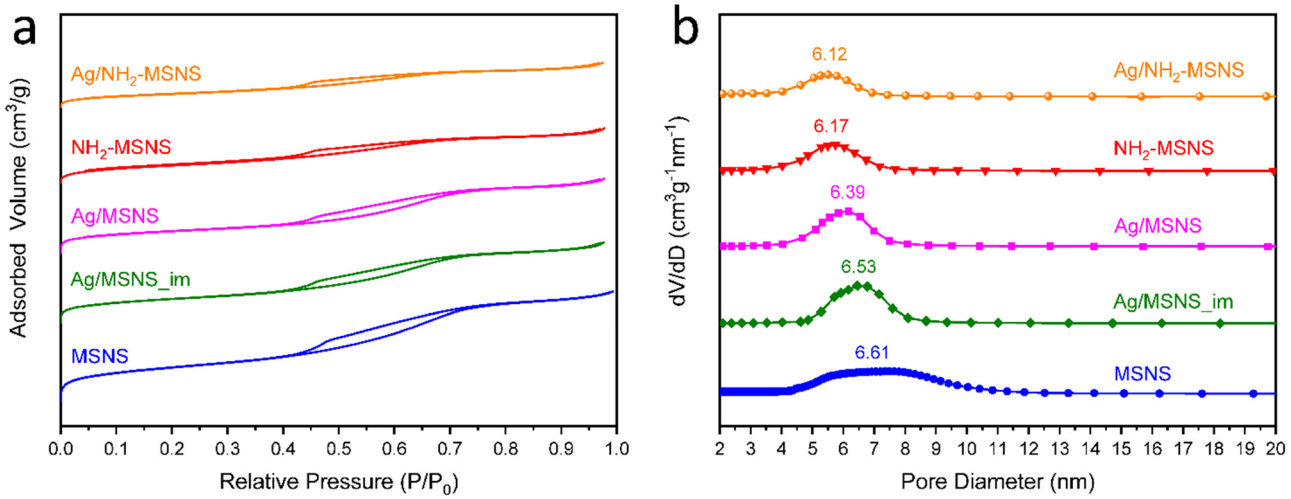

Fig. 2 (a) N_2 adsorption–desorption isotherms, and (b) BJH pore size distribution of catalysts and supports.

Table 1 The physicochemical properties of different supports and catalysts

Sample	Ag content[a] (wt%)	S_{BET}[b] ($m^2\ g^{-1}$)	V_{pore}[c] ($m^3\ g^{-1}$)	D_{pore}[d] (nm)	Ag particle size[e] (nm)	D_{Ag}[f] (%)	S_{Ag}[f] ($m^2\ g^{-1}$)	TOF (h^{-1})
MSNS	—	665	0.80	6.61	—	—	—	—
NH_2-MSNS	—	323	0.41	6.17	—	—	—	—
Ag/MSNS_im	3.0	425	0.60	6.53	8.5	14.3	2.08	78[g]
Ag/MSNS	2.5	390	0.54	6.39	6.6	20.8	2.52	135[h]
Ag/NH_2-MSNS	2.9	242	0.33	6.12	5.5	31.7	4.46	207[i]

[a] Metal loading was determined by ICP-OES. [b] Specific surface area, calculated by the BET method. [c] BJH adsorption cumulative volume of pores. [d] BJH adsorption average pore diameter. [e] Silver particle size was calculated by TEM. [f] Dispersion (D_{Ag}) and surface area of Ag (S_{Ag}) obtained from N_2O chemisorption and H_2-TPR measurements, please refer to the ESI for specific calculation details. [g] Based on a 15.3% DMO conversion under the following reaction conditions: T = 220 °C, P = 2.0 MPa, H_2/DMO = 80 and LHSV = 2.4 h^{-1}. [h] Based on a 17.1% DMO conversion under the following reaction conditions: T = 220 °C, P = 2.0 MPa, H_2/DMO = 80 and LHSV = 4.5 h^{-1}. [i] Based on a 17.4% DMO conversion under the following reaction conditions: T = 220 °C, P = 2.0 MPa, H_2/DMO = 80 and LHSV = 12.0 h^{-1}.

consistent with the feeding amount, suggesting that the active component of the catalyst fabricated by the incipient wetness impregnation method suffers almost no loss. Using MSNS as the support, the actual Ag content in the Ag/MSNS prepared by the reduction method is smaller than the feeding amount. This is attributed to the weak adsorption of Ag^+ by the -OH on the surface of MSNS, causing some Ag^+ not to be adsorbed onto the support and thereby resulting in losses. Using NH_2-MSNS as the support, the actual Ag content of Ag/NH_2-MSNS obtained by the reduction method is basically consistent with the theoretical content. This is because the introduction of $–NH_2$ on the surface of modified MSNS enhances the adsorption of Ag^+, so that Ag^+ is adsorbed on the carrier and reduced, and there is no loss in the liquid phase. The N_2 physical adsorption isotherm and BJH pore size distribution curves of the catalyst loaded with Ag are shown in Fig. 2. The types of N_2 adsorption isotherms and hysteresis loops of the three catalysts were consistent with those of the support, indicating that the loading and preparation method of Ag particles did not damage the structure of the support. However, the position and area of the hysteresis ring and the pore size distribution are all shifted in the negative direction, which indicates that the introduction of Ag particles has an effect on the physical properties of the support and reduces the pore volume and pore size. As shown in Table 1, the incorporation of Ag leads to a significant reduction in the S_{BET}, V_{pore}, and D_{pore} of the catalyst, suggesting that Ag particles have been successfully loaded onto the support. Compared with the MSNS, the pore size distributions of Ag/MSNS and Ag/MSNS_im narrow down, suggesting that the particle sizes of the Ag particles entering the pore channels of the support are relatively uniform, causing the wedge-shaped slit channels of MSNS, which are narrow on the inside and wide on the outside, to tend to be consistent. Nevertheless, it cannot be excluded that large Ag particles are attached to the surface of the support. It is notable that the D_{pore} of the Ag/NH_2-MSNS catalyst fabricated by the reduction method is essentially consistent with NH_2-MSNS, and its surface Ag dispersion is the highest (31.7), suggesting that the Ag particle size is relatively uniform and well positioned within the mesopores of the support. The phenomenon that larger particles are located outside the pores is significantly reduced.

In order to investigate the morphology characteristics and dispersion of Ag species in catalysts, TEM images and particle size distributions of Ag particles in different catalysts are shown in Fig. 3a–c. In the Ag/MSNS_im, Ag species not only occupy the nanochannels of MSNS in the form of small particles but also

© 2025 The Author(s). Published by the Royal Society of Chemistry

Open Access Article. Published on 30 May 2025. Downloaded on 1/20/2026 4:50:09 AM.
This article is licensed under a Creative Commons Attribution-NonCommercial 3.0 Unported Licence.

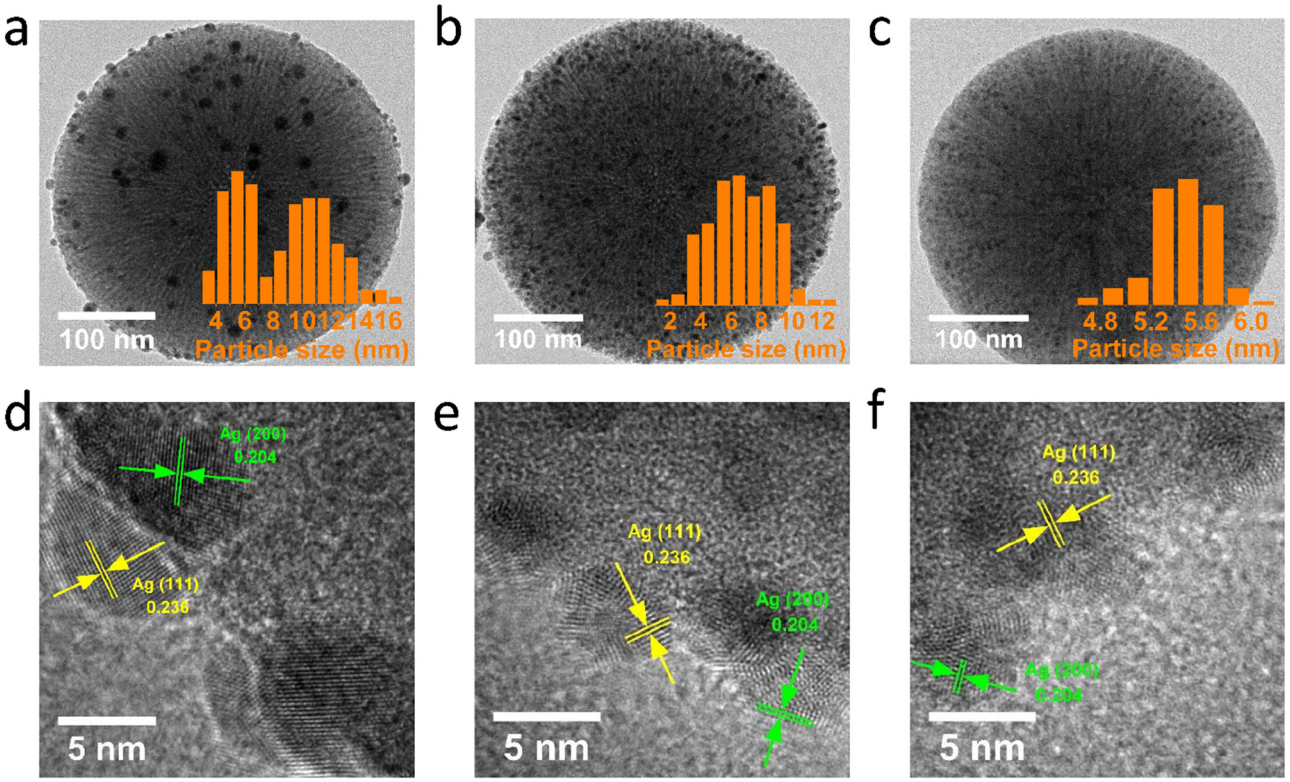

Fig. 3 TEM images of (a) Ag/MSNS_im, (b) Ag/MSNS, and (c) Ag/NH_2-MSNS catalysts, where the corresponding histograms of the Ag particle size distributions are shown in the insets. Typical high-resolution TEM images of (d) Ag/MSNS_im, (e) Ag/MSNS, and (f) Ag/NH_2-MSNS catalysts.

attach to the outer surface in the form of aggregated large particles. This implies that the catalyst fabricated by the impregnation method is liable to induce the migration and agglomeration of surface Ag nanoparticles during the calcination and reduction processes (Fig. 3a). Among them, the average diameter of Ag nanoparticles is 8.5 nm, featuring a relatively broad distribution. Furthermore, the particle size distribution is distinctly divided into two intervals: a small particle range of 3 to 8 nm and a large particle range of 7 to 17 nm. This indicates that the MSNS nanopores have a limiting effect on the migration of Ag nanoparticles, that is, in the process of calcination and reduction, the Ag species filled in the pores avoid the migration of particles at high temperature due to the limiting effect, while the Ag species attached to the outer surface migrate and agglomerate at high temperature, resulting in the interval distribution of particle size. The pore size of MSNS is 6.61 nm (Table 1), and its limiting effect is consistent with the particle size interval distribution of Ag nanoparticles.

In the Ag/MSNS catalyst, except for the small and medium-sized particles in the nanochannels of MSNS, the size of the surface aggregated particles is significantly reduced, indicating that the catalyst prepared by the reduction method largely avoided the migration and agglomeration of Ag nanoparticles (Fig. 3b). The average diameter of Ag nanoparticles decreased to 6.6 nm, the particle size was concentrated between 3 and 10 nm, and the interval distribution was not obvious, which further indicated that the agglomeration phenomenon of Ag nanoparticles larger than the MSNS aperture (6.61 nm) located on the outer surface was significantly reduced. In order to confirm whether it is the high-temperature calcination process that causes the larger Ag nanoparticles in Ag/MSNS_im, the Ag/MSNS prepared by the reduction method was calcined at 450 °C for 4 hours, and its TEM image is shown in Fig. S1b (ESI†). Compared with Ag/MSNS, the particle size of Ag nanoparticles in calcined Ag/MSNS is significantly increased. This indicates that the high-temperature calcination process can indeed increase the particle size of Ag nanoparticles, and the reason for this might stem from the Ostwald ripening process.[39,40] In the Ag/NH_2-MSNS, Ag nanoparticles are uniformly loaded in the nanoporous channels of MSNS, and no large agglomerations of Ag particles are found on the outer surface, indicating that the introduction of $-NH_2$ in MSNS plays a good control role in the growth of Ag nanoparticles during the reduction process, which is due to the complex effect of $-NH_2$ on Ag species. See the XPS and UV-vis DRS analysis below for more details. In addition, the MSNS nanoporous channels play a good limiting role for Ag nanoparticles, preventing the formation of large particles of Ag during reduction. The average diameter of Ag nanoparticles in Ag/NH_2-MSNS was 5.4 nm, and the distribution was narrow, indicating that the obtained Ag nanoparticles had a relatively uniform particle size (Fig. 3c). Compared with NH_2-MSNS, the S_{BET} and V_{pore} of Ag/NH_2-MSNS were significantly reduced, but the pore size almost did not change (Table 1), indicating that the *in situ* reduction method using NH_2-MSNS as the support obtained Ag particles in the pore rather than on the surface of the support, and further confirmed the spatial limiting effect of MSNS nanopores on Ag particles.

Open Access Article. Published on 30 May 2025. Downloaded on 1/20/2026 4:50:09 AM.
This article is licensed under a Creative Commons Attribution-NonCommercial 3.0 Unported Licence.

HRTEM was used to observe the lattice structures of Ag nanoparticles in different catalysts, as shown in Fig. 3d–f. Ag nanoparticles in Ag/MSNS_im catalysts prepared by the immersion method showed the characteristic of a long-range ordered and periodically rearranged spatial lattice structure. The same domain region covered almost the entire surface of the particles, and there were few grain boundary and lattice defects. The fringe spacings of 0.236 nm and 0.204 nm are attributed to the lattice spacing of the (111) and (200) faces of the face-centered cubic (fcc) Ag crystal, respectively (Fig. 3d). This indicates that the surface lattice of Ag nanoparticles prepared by the impregnation method is relatively complete, which is due to the migration of Ag atoms on the surface caused by the reduction of internal energy in the system during high-temperature calcination and reduction. However, the Ag nanoparticles in the Ag/MSNS and Ag/NH_2-MSNS catalysts prepared by the reduction method have a greatly reduced degree of ordered particle arrangement, and more crystal domains are distributed on the surface, with a large number of grain boundaries, lattice defects and non-uniform surfaces (Fig. 3e and f). The study of Balluffi and Seigle showed that due to the tension across the boundary, a large number of vacancies can be generated at the transverse grain boundaries.[41] In the Ag-based catalyst prepared by the liquid phase reduction method using NH_2-MSNS as the carrier, due to the complex effect of –NH_2 on Ag species and the solvent effect of ethanol, the Ag nanoparticles were stretched by electrostatic forces caused by charge separation during the growth process, resulting in atomic dislocation and the resulting grain boundaries and vacancy. The atoms near the dislocation and vacancy have higher energy, increase the valence bond unsaturated, and easily interact with the reactant molecules, showing higher activity.

3.3. Phase composition and electronic structure of the catalyst

In order to study the phase composition and crystal structure of the Ag species in the catalyst, the XRD patterns of Ag/NH_2-MSNS, Ag/MSNS, and Ag/MSNS_im catalysts are shown in Fig. 4.

The wide peaks of the three catalysts at 2θ = 23° are attributed to amorphous SiO_2 (PDF 82-0512). The XRD patterns of Ag/MSNS_im show the existence of cubic phase Ag crystals with lattice parameters $a = b = c$ = 4.0862 A, and the diffraction peaks at 2θ = 38.2°, 44.3°, 64.5° and 77.6° are attributed to the Ag 3C lattice planes (111), (200), (220) and (311), respectively (PDF 87-0597). The diffraction peak at 2θ = 33.8° is attributed to $Ag_6(Si_2O_7)$ (PDF 85-0281). Due to the large bond energy between Ag and Si atoms, Ag^+ is difficult to reduce, so the catalyst prepared by the impregnation method contains an oxidized state of Ag^+. Compared with the impregnation method, the diffraction peaks of Ag/NH_2-MSNS and Ag/MSNS prepared by the reduction method decreased significantly at 2θ = 38.2°, 44.3°, 64.5° and 77.6°. Combined with transmission electron microscopy, Ag nanoparticles are about 6 nm (Fig. 3b and c), which is much larger than the crystal face distance ((111) 2.3592 A) at 38.2° of the strongest diffraction peak of Ag 3C.

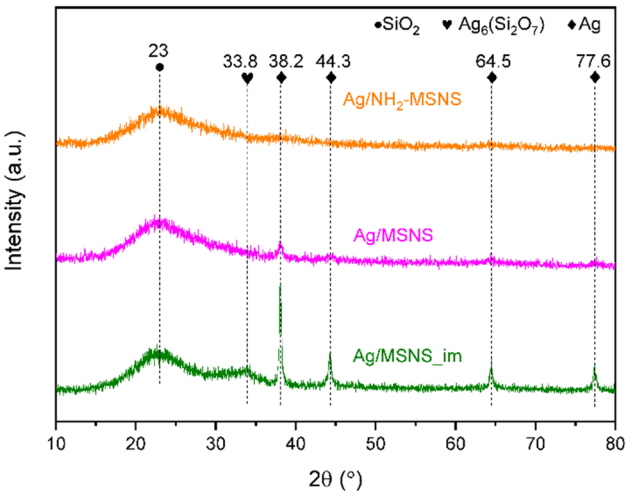

Fig. 4 XRD patterns of Ag/NH_2-MSNS, Ag/MSNS, and Ag/MSNS_im.

The above results show that Ag nanoparticles in Ag/NH_2-MSNS and Ag/MSNS catalysts are highly dispersed and amorphous, containing a large number of lattice defects and heterogeneous surfaces, which weakens the scattered X-ray interference intensity. In particular, the diffraction peak of the Ag 3C lattice surface in Ag/NH_2-MSNS almost disappeared, indicating that the introduction of –NH_2 in the MSNS further reduces the particle size of Ag nanoparticles and produces more lattice defects and heterogeneous surfaces, which is consistent with HRTEM analysis. In addition, in the catalysts Ag/NH_2-MSNS and Ag/MSNS, the diffraction peaks at 2θ = 33.8° disappear, and no diffraction peaks of other Ag species compounds exist, indicating that the reduction method can reduce all Ag precursors during the preparation of the catalyst, and no oxidation state of Ag^+ exists.

In order to further study the electronic structure and surface valence states of Ag nanoparticles in different catalysts, the X-ray photoelectron spectroscopy (XPS) of Ag 3d is shown in Fig. 5a. The spectral peaks of Ag/MSNS catalysts at the binding energies of 374.2 eV and 368.2 eV belong to the characteristic peaks of Ag $3d_{3/2}$ and Ag $3d_{5/2}$ of the elemental state Ag^0, respectively, and no chemical shift occurs, indicating that the precursor Ag species in the catalyst prepared by the reduction method using MSNS is completely reduced to the elemental state Ag^0 and no other valence species of Ag exist. The Ag/MSNS_im catalyst showed two spectral peaks at the binding energies of 374 eV and 368 eV, which were negatively shifted by 0.2 eV compared to Ag $3d_{3/2}$ and Ag $3d_{5/2}$ of Ag/MSNS. Further deconvolution of the Ag/MSNS_im spectrum shows that it is composed of the Ag 3d split energy characteristic peaks of the elemental state Ag^0 and the oxidation state Ag^+, in which the double peaks at 373.7 eV and 367.7 eV correspond to the characteristic peaks of Ag $3d_{3/2}$ and Ag $3d_{5/2}$ of Ag^+ in Ag_2O, respectively.[42] Therefore, the precursor Ag species in the catalyst prepared by the impregnation method with MSNS as the support was not completely reduced, and there was an oxidized state of Ag^+, indicating that there was a strong interaction between the silica support and Ag species. Combined

© 2025 The Author(s). Published by the Royal Society of Chemistry

Open Access Article. Published on 30 May 2025. Downloaded on 1/20/2026 4:50:09 AM. This article is licensed under a Creative Commons Attribution-NonCommercial 3.0 Unported Licence.

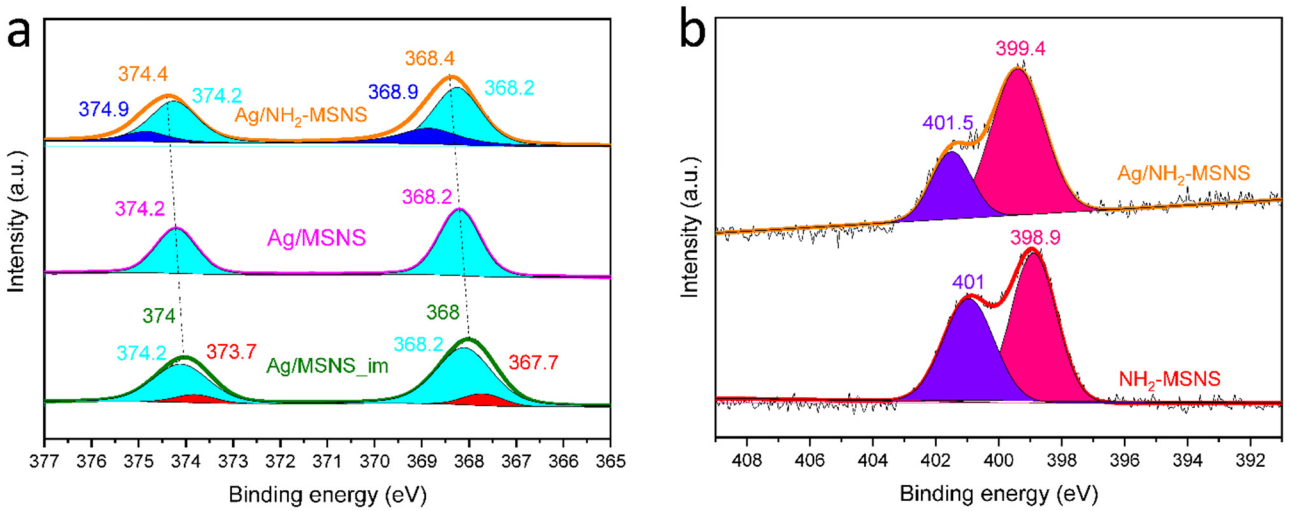

Fig. 5 (a) XPS spectra of Ag 3d in Ag/NH_2-MSNS, Ag/MSNS, and Ag/MSNS_im. (b) XPS spectra of N 1S in NH_2-MSNS and Ag/NH_2-MSNS.

with the XRD pattern, it was found that Ag^+ came from the $Ag_6(Si_2O_7)$ phase produced during the roasting process. The Ag/NH_2-MSNS catalyst has two spectral peaks at the binding energies of 374.5 eV and 368.5 eV, which are positively offset by 0.2 eV compared with Ag $3d_{3/2}$ and Ag $3d_{5/2}$ of Ag/MSNS. The spectra of Ag/NH_2-MSNS were deconvolved, and the double peaks at 374.2 eV and 368.2 eV were the Ag 3d characteristic peaks of Ag^0. The double peaks at 374.9 eV and 368.9 eV indicate that there are some Ag species in the catalyst, and the interaction between electron and nuclear charge of the Ag 3d orbital is enhanced, thus increasing the binding energy.

The X-ray photoelectron spectroscopy (XPS) of N 1s in the surface amination support NH_2-MSNS and the catalyst Ag/NH_2-MSNS are shown in Fig. 5b. The peak of NH_2-MSNS at 398.9 eV is attributed to the characteristic peak of N 1S in $-NH_2$,[43,44] and the peak at 401 eV is attributed to the characteristic peak of N 1S in protonated $-NH_3^+$.[45,46] According to the basic principle of X-ray photoelectron spectroscopy, when the density of the outer electron cloud decreases, the shielding effect of the outer electron is weakened, and the coulomb effect between the inner electron and the nucleus is enhanced, resulting in an increase in the binding energy of the inner electron. Therefore, the binding energy of N 1S in the Ag/NH_2-MSNS catalyst has a positive chemical shift of 0.5 eV compared with NH_2-MSNS, indicating that the outer electron shielding effect of N element in the NH_2-MSNS support loaded with Ag nanoparticles is weakened and it is in a state of electron loss. $-NH_2$ bonds with Ag *via* the lone pair of electrons of N, resulting in N → Ag electron transfer, and the 399.4 eV peak in Ag/NH_2-MSNS is attributed to the characteristic peak of N 1S in the $-NH_2$/Ag ligand.[47] At the same time, the peak at 401.5 eV was weakened, indicating that the interaction between Ag species and $-NH_2$ reduced the degree of protonation of $-NH_2$. Literature studies have shown that the charge transfer of electron-deprived elements to Ag changes the electron configuration of Ag 4d and 5s,p orbitals (the rehybridization of 4d → 5s,p), resulting in a decrease in the electron cloud density of valence level Ag 4d orbitals, a weakening of the shielding effect, and an increase in the Ag 3d electron binding energy of the core level.[48] Therefore, the double peaks at 374.9 eV and 368.9 eV obtained by deconvolution in the Ag/NH_2-MSNS catalyst are attributed to the Ag $3d_{2/3}$ and Ag $3d_{5/2}$ characteristic peaks of the electron-rich state $Ag^{\delta-}$, which is caused by the electron transfer of N → Ag. In summary, the contact between Ag nanoparticles and $-NH_2$ in the Ag/NH_2-MSNS catalyst generates a $-NH_2$/Ag ligand structure through the lone pair electron bonding of N. Electron transfer from N to Ag occurs in this structure, making N have an electron-deprived state and Ag an electron-rich state ($Ag^{\delta-}$).

Ultraviolet-visible diffuse reflectance spectroscopy (UV-vis DRS) is applicable for determining the charge transfer and d-orbital electron transition of transition metal ions and their complexes on the catalyst surface, thereby facilitating the study of its structure, oxidation state, and coordination state.[49] For most D-region metal nanoparticles, their diffuse reflection absorption spectra bands are continuous within the ultraviolet-visible light wavelength range.[50] The UV-vis DRS spectra of Ag/NH_2-MSNS, Ag/MSNS and Ag/MSNS_im are shown in Fig. 6.

Because the mean free path of the electrons of Ag is relatively long, the three silver catalysts have an obvious wide absorption band in the visible region (350–700 nm). They are attributed to the surface plasmon resonance (SPR) generated by photon excitation of Ag nanoparticles, whose maximum absorption peak is in the range of 400–500 nm, which is also consistent with literature reports.[51–54] According to the size quantum effect theory, when the particle size of nanomaterials is smaller, the band gap is wider, the band density is smaller, and the frequency of electron resonance is larger, which is manifested as the blue shift of the SPR spectrum. The maximum SPR absorption bands of Ag nanoparticles in Ag/NH_2-MSNS, Ag/MSNS and Ag/MSNS_im were 411 nm, 469 nm and 494 nm, respectively, and showed a redshift in sequence, indicating that Ag nanoparticles gradually increased, which was consistent with the TEM test results. The strong terminal

Open Access Article. Published on 30 May 2025. Downloaded on 1/20/2026 4:50:09 AM.
This article is licensed under a Creative Commons Attribution-NonCommercial 3.0 Unported Licence.

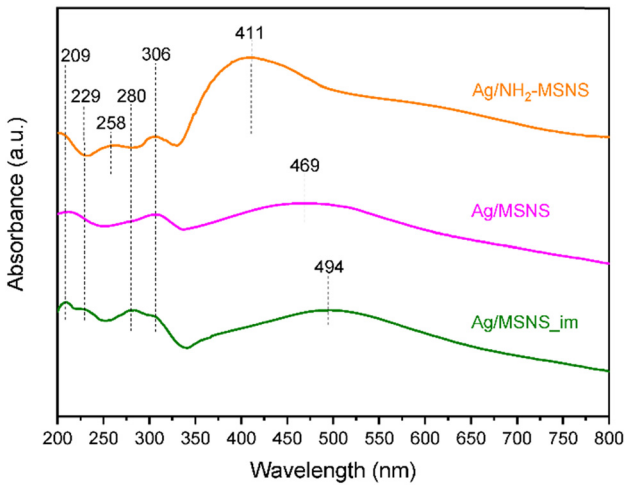

Fig. 6 UV-vis DRS spectra of Ag/NH_2-MSNS, Ag/MSNS and Ag/MSNS_im.

absorption peak of the three catalysts at 209 nm in the near ultraviolet region is attributed to the electron transfer between Si^{4+} and O^{2-} in the support SiO_2,[27] and the absorption peak at 306 nm is attributed to the SPR of the elemental Ag_n cluster.[55,56] The absorption spectra of Ag/MSNS_im in the UV region were generated at 229 nm and 280 nm. According to the literature,[56,57] the absorption peak at 229 nm is attributed to the electron transfer between isolated Ag^+ and O^{2-}, and the absorption peak at 280 nm is attributed to the SPR of the oxidation state $Ag_n^{\delta+}$ cluster. The results show that the catalyst prepared by the impregnation method contains Ag^+, an unreduced oxidation state, which comes from the $Ag_6(Si_2O_7)$ phase produced during roasting. The Ag/NH_2-MSNS and Ag/MSNS catalysts did not have absorption peaks at 229 nm and 280 nm, indicating that there was no oxidation state of Ag^+, and the Ag precursor was completely reduced during the preparation process. It is worth noting that Ag/NH_2-MSNS has an absorption spectrum at 258 nm in the ultraviolet region. Combined with XPS analysis of the Ag electron valence states of Ag/NH_2-MSNS, the absorption peak at 258 nm is attributed to the electron transfer between Ag and N. Since the electronegativity of N is smaller than that of O, the force between Ag and O is stronger. Therefore, compared with the electron transfer absorption peak between Ag^+ and O^{2-} at 229 nm, the electron transfer between N and Ag requires lower energy, resulting in a redshift phenomenon.

3.4. Adsorption and activation of reactants on catalysts

FTIR spectra of the gas-phase DMO molecule and adsorbed ones on the different catalysts at 220 °C are shown in Fig. 7a. For pure DMO, the absorption peaks at 1805 cm^{-1} and 1775 cm^{-1} are attributed to ν_{as}(C═O) and ν_s(C═O), respectively, and the absorption peaks at 1472 cm^{-1} are attributed to $\delta_{as}(CH_3)$. The absorption peaks at 1234 cm^{-1} and 1184 cm^{-1} are attributed to ν_{as}(C–O–C) and ν_s(C–O–C), respectively. For DMO adsorbed on different catalysts, the stretching vibration characteristic peaks of C═O and C–O–C showed a redshift, while the variable angle vibration characteristic peaks of CH_3 were all around 1472 cm^{-1} without displacement, indicating that the chemical adsorption of C═O and C–O–C of DMO occurred on the catalyst. The redshift of the characteristic peak of the functional group indicates that the vibration energy of the bond decreases, the bond length becomes longer, and the bond is more likely to break and undergo chemical reaction. The order of adsorption and activation of DMO by different catalysts is as follows: Ag/NH_2-MSNS > Ag/MSNS > Ag/MSNS_im. The redshift phenomenon of the DMO functional group absorption bands can be explained by molecular orbital theory: the outer electrons of the active component Ag of the catalyst enter the antibonding molecular orbital ($2\pi^*$) of C═O, thus weakening the bond energy of C═O, reducing the bond vibration energy, reducing the stability of DMO molecules and making chemical reactions easy. According to the XPS and UV-vis DRS analysis above, the Ag/MSNS_im catalyst prepared by the impregnation

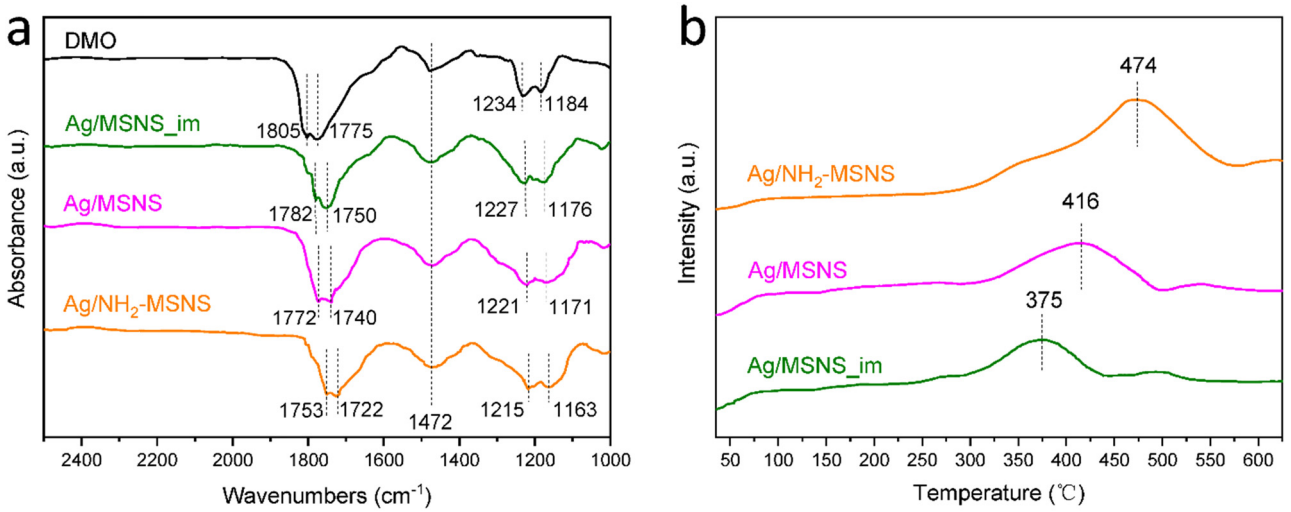

Fig. 7 (a) FTIR spectra of the gas-phase DMO molecule and *in situ* FTIR spectra of DMO adsorbed on the Ag/NH_2-MSNS, Ag/MSNS, and Ag/MSNS_im. (b) DMO-TPD data for DMO adsorbed on the Ag/NH_2-MSNS, Ag/MSNS, and Ag/MSNS_im.

© 2025 The Author(s). Published by the Royal Society of Chemistry

Open Access Article. Published on 30 May 2025. Downloaded on 1/20/2026 4:50:09 AM.
This article is licensed under a Creative Commons Attribution-NonCommercial 3.0 Unported Licence.

method contains Ag^{+} species in the oxidation state, which makes it difficult for Ag outer electrons to enter the C=O antibonding orbital, so the absorption bands of C=O and C–O–C have the smallest redshift wavenumber. The active component of the Ag/MSNS catalyst prepared by the reduction method is Ag^{0}, which makes it easier for Ag outer electrons to enter the C=O antibonding orbital, so the absorption band redshift wavenumber of C=O and C–O–C is large. The Ag/NH_2-MSNS catalyst contains electron-rich $Ag^{\delta-}$ species, which makes it easiest for Ag outer electrons to enter the C=O antibonding orbital, so the absorption bands of C=O and C–O–C have the largest redshift wavenumber. Therefore, the Ag/NH_2-MSNS catalyst has the strongest activation capacity for DMO, which is derived from the electron-rich $Ag^{\delta-}$ species generated by electron transfer from N to Ag.

Fig. 7b shows the TPD profiles for DMO adsorbed on different catalysts, in which a peak at 300–500 °C associated with DMO desorption is clearly observed. With the increase of Ag dispersion in catalysts, the adsorption capacity of DMO increased gradually. According to the desorption peak area of DMO, it can be seen that Ag/NH_2-MSNS catalyst has the largest adsorption capacity for DMO, which is due to its high Ag dispersion (31.7%). It is also noted that the desorption temperature of DMO on the Ag/NH_2-MSNS catalyst is the highest (474 °C), which is due to the enhanced adsorption of DMO by electron-rich $Ag^{\delta-}$ species, consistent with the FTIR results of DMO adsorption. The above results show that the high dispersion of Ag and the electron-rich $Ag^{\delta-}$ species in the Ag/NH_2-MSNS enhance the adsorption and activation of DMO.

In order to study the adsorption and activation of H_2 by catalysts, H_2-TPD profiles on different catalysts are shown in Fig. 8. The support MSNS and NH_2-MSNS have no H_2 desorption peak in the temperature range of 25–650 °C (not marked in the figure). On SiO_2 loaded Cu, Ag and Au nanoparticles, hot electrons generated by energy transfer between external energy and metal surface can achieve H_2 dissociation at room temperature,[58,59] and the peaks above 200 °C of the three catalysts are attributed to the desorption of H atoms adsorbed by dissociation on the surface of Ag particles.[60–62] Pundt pointed out that various defects (such as dislocations, grain boundaries, vacancies, microvoids, impurity atoms, *etc.*) in metals can form hydrogen traps for hydrogen atom diffusion.[63] Hideaki *et al.* found that hydrogen traps can attract and trap hydrogen atoms, and hydrogen atoms diffuse much faster in the dislocations and grain boundaries than in the lattice.[64,65]

Therefore, in Fig. 8, the peak in the low temperature region is attributed to the desorption of hydrogen atoms in the Ag lattice, while the peak in the high temperature region is attributed to the desorption of hydrogen atoms in the hydrogen trap at the defect of the Ag lattice. Compared with Ag/MSNS_im, the desorption peaks of Ag/NH_2-MSNS and Ag/MSNS in the low temperature region shifted to low temperature by about 30 °C, indicating that Ag nanoparticles in the catalyst prepared by the reduction method had more lattice defects, which made the diffusion of hydrogen atoms in the lattice easier, which was consistent with the lattice image analysis of HRTEM. The peak area of H_2-TPD on different catalysts represents the adsorption amount of H_2, and is positively correlated with Ag dispersion. The adsorption capacity of Ag/NH_2-MSNS on H_2 is the largest, which is due to the high Ag dispersion on its surface.

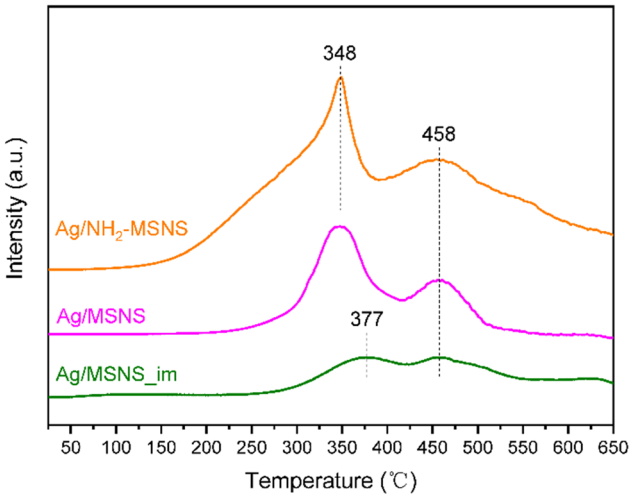

Fig. 8 H_2-TPD profiles of Ag/NH_2-MSNS, Ag/MSNS, and Ag/MSNS_im.

3.5. Catalytic performance and stability of catalysts

In the reaction of DMO catalytic hydrogenation to MG, the evaluation results of catalyst activity and stability are shown in Fig. 9. Under a certain activity of catalyst, the DMO conversion decreases with the increase of liquid-time space velocity (LHSV) (Fig. 9a). The higher conversion and the higher LHSV, the stronger activation of the catalyst. The sequence of catalytic activity of the three catalysts for DMO conversion is as follows: Ag/NH_2-MSNS > Ag/MSNS > Ag/MSNS_im. In particular, when the LHSV is lower than 1.5 h^{-1}, the Ag–NH_2-MSNS catalyst exhibits outstanding catalytic efficacy, with the DMO conversion being higher than 99%. With the increase of LHSV, the MG and EG selectivity tends to be stable around 97% and 3% respectively on the three catalysts (Fig. 9b). However, at low LHSV (<0.5 h^{-1}), the MG selectivity order of the three catalysts is Ag-MSNS_im > Ag-MSNS > Ag–NH_2-MSNS, which is opposite to that for EG. This is because DMO hydrogenation is a series reaction, the overall higher hydrogenation activity favors deep hydrogenation of MG to EG as the residence time of the mixture increases. Increasing LHSV can effectively inhibit the further conversion of MG. With the increase of LHSV, the variation trend of MG yield is consistent with the DMO conversion (Fig. 9c). The turnover frequency (TOF) sequence of DMO on the three catalysts is as follows: Ag–NH_2-MSNS (207) > Ag-MSNS (135) > Ag-MSNS_im (78) (Table 1).

Through the characterization of physical and chemical properties of different catalysts, their catalytic activities for DMO hydrogenation can be explained as follows. Compared with the impregnation method, the catalyst prepared by the reduction method has higher dispersion of Ag particles, and

Open Access Article. Published on 30 May 2025. Downloaded on 1/20/2026 4:50:09 AM.
This article is licensed under a Creative Commons Attribution-NonCommercial 3.0 Unported Licence.

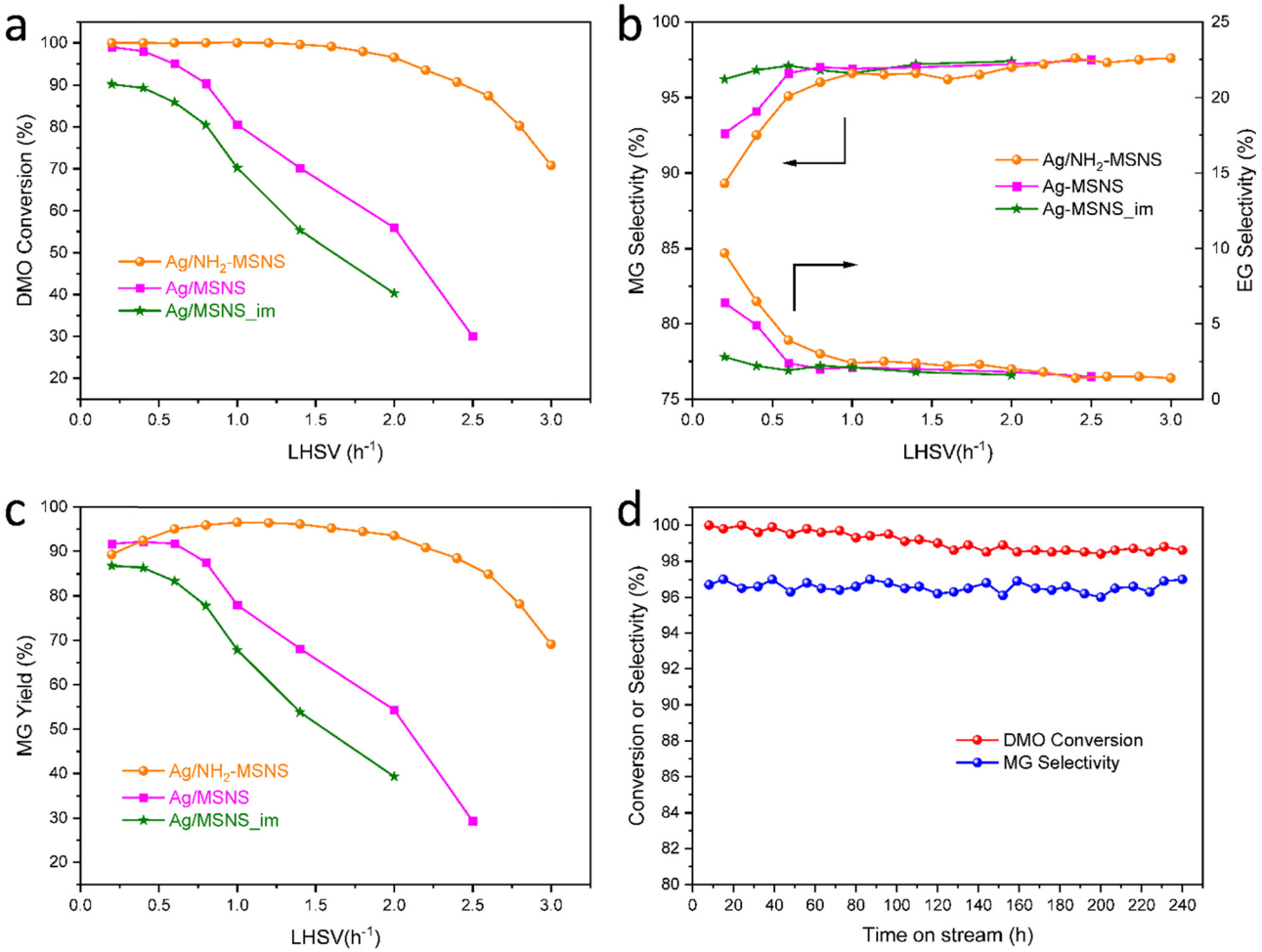

Fig. 9 (a) DMO conversion, (b) MG and EG selectivity and (c) MG yield from hydrogenation runs with the Ag/NH_2-MSNS, Ag/MSNS and Ag/MSNS_im catalysts as a function of LHSV at 220 °C under 2 MPa of H_2. (d) Kinetic data *versus* time on stream for DMO hydrogenation on the Ag/NH_2-MSNS catalyst under the following reaction conditions: T = 220 °C, P = 2.0 MPa, H_2/DMO = 80 and LHSV = 1.0 h^{-1}.

the decrease of Ag^+ species in the oxidation state enhances the adsorption and activation of DMO. At the same time, there are more lattice defects on its surface, which is more conducive to the activation and diffusion of H_2, so Ag/MSNS has higher activity. The Ag/NH_2-MSNS catalyst prepared by the reduction method using NH_2-MSNS as the support, due to the complexation of $-NH_2$, its Ag nanoparticles have smaller particle size and higher dispersion during the *in-situ* reduction growth process, and the surface lattice defects further increase, and the activation and diffusion of H_2 are further enhanced. In addition, there is electron transfer between $-NH_2$ and Ag species on the support surface, and the electron-rich $Ag^{\delta-}$ is more likely to adsorb DMO and activate the C=O bond. Therefore, the high activity of the Ag/NH_2-MSNS catalyst is due to its highly dispersed Ag active components, large number of lattice defects, and electron-rich $Ag^{\delta-}$ species. Under the reaction conditions of P = 2.0 MPa, T = 220 °C, H_2/DMO = 80 and LHSV = 1.0 h^{-1}, the DMO conversion and MG selectivity of the Ag/NH_2-MSNS catalyst in the optimal state were 100% and 96.6% respectively.

The stability test results of the Ag/NH_2-MSNS catalyst for DMO hydrogenation are shown in Fig. 9d. After 250 h reaction, the selectivity of MG remained basically unchanged, stable at about 96.5%. Compared with almost 100% at the beginning of the reaction, the conversion rate of DMO decreased slightly to 98.5%, and stabilized after 250 h, and the MG yield was above 95%. This shows that the Ag/NH_2-MSNS catalyst has excellent catalytic activity, selectivity and stability in the reaction of DMO hydrogenation to prepare MG. The slight reduction in the conversion rate may be due to subtle changes in the surface structure of Ag nanoparticles during the reaction.

4. Conclusions

In summary, using mesoporous silica nanospheres (MSNS) with uniform center-radial mesopore channels (~7 nm) as the support, $-NH_2$ was successfully introduced for surface functionalization, and the Ag/NH_2-MSNS catalyst with an Ag dispersion of 0.317 and a content of 3 wt% was prepared by the *in situ* reduction method. In the reaction of selective hydrogenation of DMO to MG, under the conditions of P = 2.0 MPa, T = 220 °C, H_2/DMO molar ratio = 80, and LHSV = 1.0 h^{-1}, the best catalytic state achieved a DMO conversion of 100%, a MG

© 2025 The Author(s). Published by the Royal Society of Chemistry

Open Access Article. Published on 30 May 2025. Downloaded on 1/20/2026 4:50:09 AM. This article is licensed under a Creative Commons Attribution-NonCommercial 3.0 Unported Licence.

selectivity of 96.6%, a TOF as high as 207, and the MG yield could still remain above 95% after a 250 h lifetime investigation. Characterization findings indicate that the easily accessible highly dispersed Ag active components, the lattice defects which are conducive to the adsorption, activation and diffusion of H_2, and the electron-rich $Ag^{\delta-}$ species that facilitate the adsorption and activation of DMO are the reasons why the catalyst possesses relatively high activity, selectivity and stability.

Author contributions

Guilin Dong: conducting a research and investigation process, specifically performing the experiments, or data/evidence collection. Preparation, creation and presentation of the published work, specifically writing the initial draft (including substantive translation). Haiyong Wang: development or design of methodology; creation of models. Verification, whether as a part of the activity or separate, of the overall replication/reproducibility of results/experiments and other research outputs. Qian Jiang: application of statistical, mathematical, computational, or other formal techniques to analyse or synthesize study data. Yuhe Liao: preparation, creation and presentation of the published work by those from the original research group, specifically critical review, commentary or revision – including pre- or post-publication stages. Chenguang Wang: Ideas; formulation or evolution of overarching research goals and aims. Acquisition of the financial support for the project leading to this publication. Management and coordination responsibility for the research activity planning and execution. Provision of study materials, reagents, materials, patients, laboratory samples, animals, instrumentation, computing resources, or other analysis tools. Oversight and leadership responsibility for the research activity planning and execution, including mentorship external to the core team. All the authors discussed the results and reviewed the manuscript.

Data availability

All the experimental data are included in the main text and the ESI.†

Conflicts of interest

There are no conflicts to declare.

Acknowledgements

This work was financially supported by the National Natural Science Foundation of China (No. 52276220).

Notes and references

1 J. Qiu, G.-Q. Yang, J. Zuo, X. Liu, Z. Lan, W. Chen, Z.-W. Liu and Y. Yuan, *J. Catal.*, 2024, **435**, 115547.
2 H. Wang, T. Lan, G. Zhao, G. Chen and Y. Lu, *ACS Catal.*, 2024, **14**, 728–740.
3 Y. Wang, H. Yang, B. Li, S. Liu, M. He, Q. Chen and J. Li, *Int. J. Mol. Sci.*, 2022, **23**, 11074.
4 Y. Sun, H. Wang, J. Shen, H. Liu and Z. Liu, *Catal. Commun.*, 2009, **10**, 678–681.
5 Y. Xu, W. Dou, Y. Zhao, G. Huang and X. Ma, *Ind. Eng. Chem. Res.*, 2012, **51**, 11653–11658.
6 Q. Xu, *Coord. Chem. Rev.*, 2002, **231**, 83–108.
7 T. Turek, D. L. Trimm and N. W. Cant, *Catal. Rev.*, 1994, **36**, 645–683.
8 R. Angamuthu, P. Byers, M. Lutz, A. L. Spek and E. Bouwman, *Science*, 2010, **327**, 313–315.
9 Y. Weng, M. Zou, X. Liu, J. Gu, Z. Liu, Y. Fan, Y. Zhang and Y. Liao, *Chem. Commun.*, 2023, **59**, 4340–4343.
10 F. Zheng, J. Gong, H. Zhang, W. Shu, X. Wang, S. Qin, C. Zhang and B. Dai, *Chem. Eng. J.*, 2024, **492**, 152350.
11 Q. Yang, Y. Fan, C. Liu, J. Zhou, L. Zhao and H. Zhou, *Energy*, 2023, **277**, 127668.
12 L. Song, Y. He, C. Zhou, G. Shu, K. Ma and H. Yue, *Chem. Commun.*, 2022, **58**, 11657–11660.
13 Y. Sun, K. Fu, J. Wei, Q. Ge, Q. Ma, G. Wang and J. Sun, *ACS Catal.*, 2024, **14**, 18744–18752.
14 Z. Li, Y. Li, X. Wang, Y. Tan, W. Yang, H. Zhu, X. Chen, W. Lu and Y. Ding, *Chem. Eng. J.*, 2023, **454**, 140001.
15 J. Gong, H. Zhang, W. Shu, F. Zheng, C. Zhang, H. Wang, N. Zhang and B. Dai, *Green Chem.*, 2024, **26**, 5966–5976.
16 F. S. Rohman, S. H. Syed Sulaiman and N. Aziz, *Int. J. Hydrogen Energy*, 2021, **46**, 30882–30890.
17 Y. Fang, H. Sun, B. Ma and C. Zhao, *J. Catal.*, 2022, **407**, 44–53.
18 J. Zhu, G. Zhao, C. Meng, P. Chen, X.-R. Shi and Y. Lu, *Chem. Eng. J.*, 2021, **426**, 130857.
19 J. Xu, Z.-C. Long, Z.-C. Chen, C.-F. Zhu, H.-G. Xu, J.-W. Zheng, E. Janssens, W.-J. Zheng, G.-L. Hou and S.-Y. Xie, *ACS Catal.*, 2024, **14**, 14733–14743.
20 Q.-N. Wang, R. Duan, Z. Feng, Y. Zhang, P. Luan, Z. Feng, J. Wang and C. Li, *ACS Catal.*, 2024, **14**, 1620–1628.
21 L. Wu, M. Guo, X. Xu, J. Ding and Q. Zhong, *J. Environ. Chem. Eng.*, 2024, **12**, 113037.
22 C. Liu, L. Zhao, S. Zhu, Y. Shen, J. Yu and Q. Yang, *Energy*, 2023, **282**, 128790.
23 Z. Luo, X. Xu, G. Dong, Y. Cao, S. Hu, G. Ye, Y.-A. Zhu, J. Zhou, W. Li and X. Zhou, *Chem. Eng. J.*, 2022, **450**, 138397.
24 G. Dong, Z. Luo, Y. Cao, S. Zheng, J. Zhou, W. Li and X. Zhou, *J. Catal.*, 2021, **401**, 252–261.
25 J. Zheng, X. Duan, H. Lin, Z. Gu, H. Fang, J. Li and Y. Yuan, *Nanoscale*, 2016, **8**, 5959–5967.
26 M. Ouyang, Y. Wang, J. Zhang, Y. Zhao, S. Wang and X. Ma, *RSC Adv.*, 2016, **6**, 12788–12791.
27 A. Yin, C. Wen, W.-L. Dai and K. Fan, *Appl. Catal., B*, 2011, **108–109**, 90–99.
28 J. Zheng, H. Lin, X. Zheng, X. Duan and Y. Yuan, *Catal. Commun.*, 2013, **40**, 129–133.
29 M. M.-J. Li, L. Ye, J. Zheng, H. Fang, A. Kroner, Y. Yuan and S. C. E. Tsang, *Chem. Commun.*, 2016, **52**, 2569–2572.

© 2025 The Author(s). Published by the Royal Society of Chemistry

Open Access Article. Published on 30 May 2025. Downloaded on 1/20/2026 4:50:09 AM. This article is licensed under a Creative Commons Attribution-NonCommercial 3.0 Unported Licence.

30 J. Zheng, H. Lin, Y.-N. Wang, X. Zheng, X. Duan and Y. Yuan, *J. Catal.*, 2013, **297**, 110–118.
31 J. Zhou, X. Duan, L. Ye, J. Zheng, M. M.-J. Li, S. C. E. Tsang and Y. Yuan, *Appl. Catal., A*, 2015, **505**, 344–353.
32 M. Hu, Y. Yan, X. Duan, L. Ye, J. Zhou, H. Lin and Y. Yuan, *Catal. Commun.*, 2017, **100**, 148–152.
33 H. Chen, J. Tan, J. Cui, X. Yang, H. Zheng, Y. Zhu and Y. Li, *Mol. Catal.*, 2017, **433**, 346–353.
34 G. Dong, Y. Cao, S. Zheng, J. Zhou, W. Li, F. Zaera and X. Zhou, *J. Catal.*, 2020, **391**, 155–162.
35 D. Shen, J. Yang, X. Li, L. Zhou, R. Zhang, W. Li, L. Chen, R. Wang, F. Zhang and D. Zhao, *Nano Lett.*, 2014, **14**, 923–932.
36 X. Xu, X. Hu, Z. Luo, Y. Cao, Y.-A. Zhu, W. Li, J. Zhou and X. Zhou, *New J. Chem.*, 2023, **47**, 6045–6049.
37 C. J. G. Van Der Grift, A. F. H. Wielers, B. P. J. Jogh, J. Van Beunum, M. De Boer, M. Versluijs-Helder and J. W. Geus, *J. Catal.*, 1991, **131**, 178–189.
38 M. Boudart, *Chem. Rev.*, 1995, **95**, 661–666.
39 S. C. Parker and C. T. Campbell, *Phys. Rev. B: Condens. Matter Mater. Phys.*, 2007, **75**, 035430.
40 R. van den Berg, T. E. Parmentier, C. F. Elkjær, C. J. Gommes, J. Sehested, S. Helveg, P. E. de Jongh and K. P. de Jong, *ACS Catal.*, 2015, **5**, 4439–4448.
41 R. W. Balluffi and L. L. Seigle, *Acta Mater.*, 1957, **5**, 449–454.
42 V. K. Kaushik, *J. Electron Spectrosc. Relat. Phenom.*, 1991, **56**, 273–277.
43 B. J. Lindberg and J. Hedman, *Chem. Scr.*, 1975, **7**, 155–166.
44 M. Barber, J. A. Connor, L. M. R. Derrick, M. B. Hall and I. H. Hillier, *J. Chem. Soc., Faraday Trans.*, 1973, **69**, 559–562.
45 D. S. Everhart and C. N. Reilley, *Surf. Interface Anal.*, 1981, **3**, 258–268.
46 T. Yoshida and S. sawada, *Bull. Chem. Soc. Jpn.*, 1974, **47**, 50–53.
47 D. M. Thornburg and R. J. Madix, *Surf. Sci.*, 1990, **226**, 61–76.
48 W. F. Egelhoff, *Surf. Sci. Rep.*, 1987, **6**, 253–415.
49 P. Morozzi, B. Ballarin, S. Arcozzi, E. Brattich, F. Lucarelli, S. Nava, P. J. Gómez-Cascales, J. A. G. Orza and L. Tositti, *Atmos. Environ.*, 2021, **252**, 118297.
50 J. A. Creighton and D. G. Eadon, *J. Chem. Soc., Faraday Trans.*, 1991, **87**, 3881–3891.
51 P. Prieto, V. Nistor, K. Nouneh, M. Oyama, M. Abd-Lefdil and R. Díaz, *Appl. Surf. Sci.*, 2012, **258**, 8807–8813.
52 Y. Wang, Y. Zheng, C. Z. Huang and Y. Xia, *J. Am. Chem. Soc.*, 2013, **135**, 1941–1951.
53 N. G. Bastús, F. Merkoçi, J. Piella and V. Puntes, *Chem. Mater.*, 2014, **26**, 2836–2846.
54 S. H. Im, Y. T. Lee, B. Wiley and Y. Xia, *Angew. Chem., Int. Ed.*, 2005, **44**, 2154–2157.
55 K.-i Shimizu and A. Satsuma, *Phys. Chem. Chem. Phys.*, 2006, **8**, 2677–2695.
56 K.-i Shimizu, J. Shibata, H. Yoshida, A. Satsuma and T. Hattori, *Appl. Catal., B*, 2001, **30**, 151–162.
57 K. A. Bethke and H. H. Kung, *J. Catal.*, 1997, **172**, 93–102.
58 S. Mukherjee, L. Zhou, A. M. Goodman, N. Large, C. Ayala-Orozco, Y. Zhang, P. Nordlander and N. J. Halas, *J. Am. Chem. Soc.*, 2014, **136**, 64–67.
59 Z. Yin, Y. Wang, C. Song, L. Zheng, N. Ma, X. Liu, S. Li, L. Lin, M. Li, Y. Xu, W. Li, G. Hu, Z. Fang and D. Ma, *J. Am. Chem. Soc.*, 2018, **140**, 864–867.
60 S. Xia, L. Zheng, W. Ning, L. Wang, P. Chen and Z. Hou, *J. Mater. Chem. A*, 2013, **1**, 11548–11552.
61 H. Wilmer, T. Genger and O. Hinrichsen, *J. Catal.*, 2003, **215**, 188–198.
62 F. Arena, G. Italiano, K. Barbera, S. Bordiga, G. Bonura, L. Spadaro and F. Frusteri, *Appl. Catal., A*, 2008, **350**, 16–23.
63 A. Pundt and R. Kirchheim, *Annu. Rev. Mater. Res.*, 2006, **36**, 555–608.
64 H. Iwaoka, T. Ide, M. Arita and Z. Horita, *Int. J. Hydrogen Energy*, 2017, **42**, 24176–24182.
65 H. Iwaoka, M. Arita and Z. Horita, *Acta Mater.*, 2016, **107**, 168–177.

© 2025 The Author(s). Published by the Royal Society of Chemistry